COMMUNICATIONS IN COMPUTATIONAL PHYSICS
Vol. **5**, No. 5, pp. 986-1011

Commun. Comput. Phys.
May 2009

A Weighted Multi-Domain Spectral Penalty Method with Inhomogeneous Grid for Supersonic Injective Cavity Flows

Wai-Sun Don[1], David Gottlieb[1] and Jae-Hun Jung[2,*]

[1] *Division of Applied Mathematics, Brown University, Providence, RI 02912, USA.*
[2] *Department of Mathematics, University of Massachusetts at Dartmouth, North Dartmouth, MA 02747-2300, USA.*

Received 16 December 2007; Accepted (in revised version) 16 September 2008

Communicated by Jan S. Hesthaven

Available online 20 October 2008

Abstract. In [*J. Comput. Phys.* **192(1)**, pp.325-354 (2003)], we have developed a multi-domain spectral method with stable and conservative penalty interface conditions for the numerical simulation of supersonic reactive recessed cavity flows with homogeneous grid. In this work, the previously developed methodology is generalized to inhomogeneous grid to simulate the two dimensional supersonic injector-cavity system. Non-physical modes in the solution generated at the domain interfaces due to the spatial grid inhomogeneity are minimized using the new weighted multi-domain spectral penalty method. The proposed method yields accurate and stable solutions of the injector-cavity system which agree well with experiments qualitatively. Through the direct numerical simulation of the injector-cavity system using the weighted method, the geometric effect of the cavity wall on pressure fluctuations is investigated. It is shown that the recessed slanted cavity attenuates pressure fluctuations inside cavity enabling the cavity to act potentially as a stable flameholder for scramjet engine.

AMS subject classifications: 65M12, 65M70, 76J20

Key words: Penalty interface conditions, weighted multi-domain spectral penalty methods, supersonic recessed cavity flame-holder, compressible Navier-Stokes equations.

1 Introduction

Spectral methods have been actively used in the computational fluid dynamics community in the last decades due to the merit of high order accuracy maintained for long time

*Corresponding author. *Email addresses:* wsdon@dam.brown.edu (W.-S. Don), dig@dam.brown.edu (D. Gottlieb), jaehun@buffalo.edu (J.-H. Jung). The current address of Jae-Hun Jung: Department of Mathematics, The State University of New York at Buffalo, Buffalo, NY 14260-2900.

integration. Spectral methods have been also applied to highly complex fluid systems and have been proven to yield accurate solutions even with the stiff or discontinuous spatial gradients. These systems include the supersonic shock bubble interactions [12], the supersonic cavity flows [11], the Ritchmyer-Meshkov instability [20, 21] and etc. The difficulty of implementing the spectral method to these complex fluid systems is to deal with the nonsmooth spatial gradients successfully. The discontinuous solution is commonly found in most high speed fluid mechanical systems. The spectral approximation of such solution yields spurious oscillations near the discontinuity, known as the Gibbs phenomenon. These Gibbs oscillations deteriorate both the accuracy and stability in general. The essential methodology to deal with such oscillations in the spectral solution is the spectral viscosity or filtering methods [5, 16, 22, 25]. The filtering which is mathematically equivalent to the spectral viscosity method but practically more efficient, is used to stabilize the flow fields over the time integration. The filtering reduces the high order oscillations by attenuating the high modes in the solution. The filtering method can be applied either globally or locally. By applying the filtering locally one can obtain more accurate solution in the smooth region. Thus it is desirable to separate the locally nonsmooth regions from the global smooth region. A multi-domain spectral method has been developed to address this problem [8, 11, 13, 14, 17–19], with which the physical domain is split into multiple subdomains. For the multi-domain spectral method, the proper interface conditions should be imposed at the domain interfaces. The simplest condition is the averaging method. With the averaging method, the flow field at the domain interface is obtained by averaging the two adjacent solutions across the interface. Thus the continuity of the solution is ensured with the averaging method. Although this method is simple and efficient to be implemented, it may cause the generation of nonphysical solutions at the interface if the two adjacent subdomains have different grid resolutions near the interface, i.e. if the grid system is inhomogeneous. We define the grid *inhomogeneity* as the grid configuration such that the grid resolutions between the adjacent subdomains across the domain interface are different. Such difference can be obtained by having each domain have either different order of polynomials or different domain length. If the grid distribution is inhomogeneous, the stable interface conditions derived for the homogeneous grid system are not enough and one needs to find the conditions with which the spatial inhomogeneity can be addressed properly.

At the domain interface of two adjacent subdomains which have the degree of polynomials, N_1 and N_2, and the domain lengths Δ^I and Δ^{II} in the x-direction, respectively, the ratio of the grid spacing between Δx_1 and Δx_2 at the interface is approximately given by

$$\frac{\Delta x_2}{\Delta x_1} = \frac{\Delta^{II}}{\Delta^I} \cdot \frac{N_1^2}{N_2^2}. \tag{1.1}$$

If the grid spacing ratio $\Delta x_2/\Delta x_1$ is different and far from unity, we consider it as the inhomogeneous grid system. If $\Delta x_2/\Delta x_1 = 1$, the grid is homogeneous, and the averaging method can play an efficient role as a stable interface condition. However, if the ratio

is far from unity, the simple averaging interface condition can cause the growth of the solution at the domain interface. In the real computation, the values of N_1, N_2 and Δ^I, Δ^{II} are chosen such that $\Delta x_2/\Delta x_1$ becomes close to unity. The current work centers around the development of the method dealing with the solution in inhomogeneous grid system, i.e., when $\Delta x_2/\Delta x_1 \neq 1$.

In [11], we performed a 2D direct numerical simulation (DNS) of the recessed cavity flows with the multi-domain spectral penalty method under the condition that the grid is *homogeneous*. In [11], the spacing and the number of collocation points in each subdomain are the same in each dimension. In this study, we extend the previous work to the inhomogeneous grid system to consider the injector-cavity system with the local hydrogen fuel injector. The crucial part of the DNS of the injector-cavity system is to resolve the hydrogen jet injector without causing any instability or nonphysical growing modes at the domain interfaces. The ratio of the injector to the cavity length scale is about $\mathcal{O}(10^{-1})$. We use a smaller subdomain with higher order polynomials to resolve the hydrogen jet. In Fig. 1 the local domain configuration is shown for the cavity flameholder with (left figure) and without (right figure) the injector. The local domain configuration shown in the right figure is the typical domain system used in [11] for which the homogeneous grid system is used. The grid system in the left figure is inhomogeneous as the local injector is placed in the narrow domain.

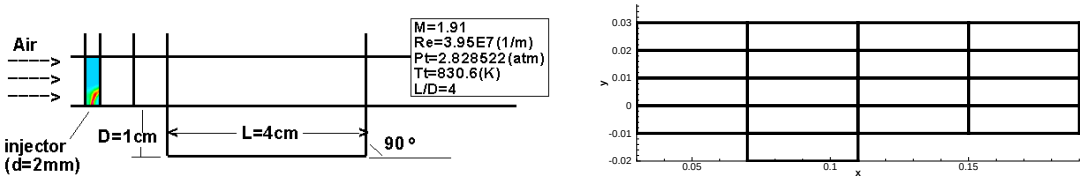

Figure 1: Left: Local domain configuration of the normal injector-cavity flame-holder. Right: Local domain configuration of the normal cavity without injector. The initial physical configuration of the injector-cavity flame-holder is given in the legend box, where M denotes the Mach number, Re the normalized Reynolds number, P_t the baseline total pressure, T_t the baseline total temperature, and L/D the length to depth ratio of cavity.

In [11], the stability analysis has been done with the assumption that each subdomain has the same length but can have different polynomial orders. With different polynomial orders, the stability is still maintained. In this work, we further show that the stability can be also maintained with the different domain length. That is, the stability can be obtained for fully inhomogeneous grids.

The stability conditions obtained are only necessary conditions. There can be nonreflecting modes in the solution at the inhomogeneous domain interface that can yield a growth in time. A weighted spectral penalty method is proposed in order to minimize such nonphysical reflecting modes. We note that in [8] the multidomain spectral method has been also used for the localized incompressible stratified turbulence flows in which the strong adaptive averaging method has been used with the spectral filtering technique. In our work, we observe that the averaging method with the filtering technique does not

yield a smooth profile across the inhomogeneous grid interface for the compressible supersonic flows. This is due to the fact that the averaging method does not guarantee the stability for the inhomogeneous grid as shown in the following sections. The major developments of the current work are as follows:

- A generalized conservative and stable penalty conditions are derived for the inhomogeneous grid system.
- The weighted spectral penalty method is developed to minimize the non-physical growth modes at the inhomogeneous domain interfaces.

Here we note that the 2D extension of the weighted penalty method is mainly based on the 1D method without a full consideration of corners in 2D geometry. As we will mention in the paper, however, the numerical experiments indicate that the proposed model based on the 1D method is stable and accurate.

Using the proposed weighted penalty method, we carry out the 2D DNS of the injector-cavity system. Cavity is an efficient flame-holder of scramjet engine as it generates the self-sustained recirculation region. The hot radicals from the chemical reactions residing in the recirculation region reduce the induction time and consequently maintain the auto-ignition. For the continuous auto-ignition and better fuel efficiency, such recirculation region should be stable for long time. In addition to the recirculation, the self-sustained acoustic oscillations bouncing back and forth inside cavity disturb the recirculation generating pressure fluctuations. The geometry of cavity is an important parameter for maintaining a stable recirculation while reducing the pressure oscillations. It is shown in [11] that the recessed cavity flameholder reduces the pressure fluctuations inside cavity more considerably than the normal wall cavity. In this research we verify qualitatively that the recessed cavity increases the stability of the recirculation and reduces the pressure fluctuations inside the recessed cavity with the hydrogen injector. For the 2D DNS, we use the grid inhomogeneity by having the different domain lengths while the same polynomial order in each domain is used. The full grid inhomogeneity can be also used, that is, the order and length of each domain can be all different. Our numerical experiments show that the results are all similar for both cases. Without loss of generality, the numerical simulation of the injector-cavity system is conducted with the domain lengths different but the orders the same.

The paper is organized as follows. In Section 2, a Legendre multi-domain spectral method with the inhomogeneous grid is explained. Stability and conservativity are derived with the grid inhomogeneity. The generalized penalty interface conditions are derived accordingly. The weighted penalty method is proposed and various examples are illustrated. In Section 3, the governing equations and the injector-cavity system are briefly described. The numerical results from the simulation of the supersonic cavity flame-holder are provided. In this section, we verify that the proposed weighted spectral penalty method successfully works with the inhomogeneous grid of the injector-cavity system. The pressure fluctuations both in the normal and 30° wall cavities are presented. Concluding remarks with a brief future work outline are given in Section 4.

2 Multi-domain spectral method with inhomogeneous local mesh refinement

2.1 Conservative spectral penalty methods for inhomogeneous grid

In this section, we will consider the spectral penalty method for the inhomogeneous grid. We consider the following one-dimensional conservation laws:

$$\frac{\partial q(x,t)}{\partial t}+\frac{\partial f(q(x,t))}{\partial x}=0,\quad q(x,t):\mathbb{R}\times\mathbb{R}\to\mathbb{R}^n,\quad x\in\mathbb{R},\quad t>0. \tag{2.1}$$

Here $q(x,t)$ and $f(q(x,t))$ are the state and flux vectors respectively with n components each. In [6] the conservative multi-domain Legendre method was proposed to approximate (2.1) on the Legendre Gauss-Lobatto collocation points and such formulation was successfully used in [11]. In [6], theorems for the multi-domain Legendre penalty method have been derived under the assumption that each subdomain has the same domain length but the polynomial orders of approximation can be different. The different polynomial order in each domain makes the grid system inhomogeneous. Thus the same polynomial order has been used for the numerical simulation in [11] to avoid any numerical artifacts due to such grid inhomogeneity. In this paper, we will further generalize the previous formulation for fully inhomogeneous grid system.

For simplicity, we consider two subdomains $\Omega^I=[x_L,0]$ and $\Omega^{II}=[0,x_R]$, for which the domain interface is at $x=0$ and $x_L<0$ and $x_R>0$. In [11], $x_L=-x_R=-2$, but $|x_L|$ and x_R can be different in this paper. Furthermore the left domain uses the polynomial order of N and the right domain of M. Note that N is not necessarily the same as M. The Legendre multi-domain spectral penalty method is then given by

$$\begin{aligned}\frac{\partial q_N^I}{\partial t}+\frac{\partial I_N^I f(q_N^I)}{\partial x}=&\mathcal{B}(q_N^I(x_L,t))+SV(q_N^I)+\tau_1 Q_N(x)[f^+(q_N^I(0,t))-f^+(q_M^{II}(0,t))]\\&+\tau_2 Q_N(x)[f^-(q_N^I(0,t))-f^-(q_M^{II}(0,t))],\end{aligned} \tag{2.2a}$$

$$\begin{aligned}\frac{\partial q_M^{II}}{\partial t}+\frac{\partial I_M^{II} f(q_M^{II})}{\partial x}=&\mathcal{B}(q_M^{II}(x_R,t))+SV(q_M^{II})+\tau_3 Q_M(x)[f^+(q_M^{II}(0,t))-f^+(q_N^I(0,t))]\\&+\tau_4 Q_M(x)[f^-(q_M^{II}(0,t))-f^-(q_N^I(0,t))].\end{aligned} \tag{2.2b}$$

Here q_N^I denotes the numerical approximation of $q(x,t)$ in Legendre polynomial of order N in Ω^I and q_M^{II} of order M in Ω^{II}. $\mathcal{B}$ is the boundary operator at the end points, i.e., $x=x_L,x_R$ and SV is the spectral vanishing-viscosity terms. I_N^I and I_M^{II} are the Legendre interpolation operators for the left and right subdomains respectively. Q_N and Q_M are the polynomials of order N and M respectively defined to vanish at the collocation points except at the boundary or interface points, that is, for example, for Ω^I, $Q_N(x_i)=0$ for $i=1,\cdots,N-1$ and $Q_N(x_i)=1$ for $i=0,N$. The positive and negative fluxes f^+ and f^- are defined by

$$f^{\pm}=\int S\Lambda^{\pm}S^{-1}dq, \tag{2.3}$$

with

$$A \equiv \frac{\partial f}{\partial q} = S\Lambda S^{-1}. \tag{2.4}$$

The Jacobian matrix $A \in \mathbb{R}^{n\times n}$ is assumed to be symmetric. Λ^+ and Λ^- are the diagonal matrices composed of positive and negative eigenvalues of A respectively such as $\Lambda = \Lambda^+ + \Lambda^-$, $\Lambda \in \mathbb{R}^{n\times n}$ such that $A^{\pm} = S\Lambda^{\pm}S^{-1}$. S and Λ are the variables related to the characteristics and its direction and speed of propagation, the similarity and eigenvalue matrices respectively. τ_1, τ_2, τ_3 and τ_4 are the penalty parameters and all are constants. As in [11], we assume that the boundary terms and the spectral vanishing-viscosity terms do not cause any instabilities and they do not appear in the following analysis. For the following theorems we define the discrete Legendre norm

$$(p,q)_N := \sum_{i=0}^{N} p(x_i)q(x_i)\omega_i,$$

where x_i are the Legendre Gauss-Lobatto collocation points and

$$\omega_i = \frac{2}{N(N+1)[L_N(\xi(x_i))]^2}.$$

Here ξ is the linear map from x to the Legendre Gauss-Lobatto points over $[-1,1]$. If $pq \in P_{2N-1}$, the discrete sum is exact, i.e.,

$$(p,q)_N = \int_{-1}^{1} p(\xi(x))q(\xi(x))d\xi.$$

In the following analysis, we define the weight vector $\vec{\omega}_N^I$ as the weight vector in Ω^I with $N+1$ components such as $\vec{\omega}_N^I = (\omega_0^I, \cdots, \omega_N^I)^T$, where ω_i^I is ω_i in Ω^I and $\omega_i^{II} = \omega_i$ in Ω^{II}. We note that ω_0^I and ω_N^I without the vector symbol denote the first and last components of $\vec{\omega}_N^I$.

Theorem 2.1 (Conservation, [6]). *The scheme given in* (2.2) *is conservative if* $x_L = -x_R = -2$ *and the penalty parameters satisfy the following conditions*

$$\tau_1\omega_N^I - \tau_3\omega_M^{II} = 1, \quad \tau_2\omega_N^I - \tau_4\omega_M^{II} = 1. \tag{2.5}$$

Here we note that there is a typo in the first equation of Eq. (23) on page 332 in [11]. The second term in the equation should not be $\tau_1\omega_M^{II}$ but should be $\tau_3\omega_M^{II}$ as given in the theorem above.

Theorem 2.2 (Stability, [6]). *The scheme* (2.2) *is stable if* $x_L = -x_R = -2$ *and the penalty parameters satisfy the followings*

$$2\tau_1\omega_N^I \le 1, \quad 2\tau_2\omega_N^I \ge 1, \quad 2\tau_3\omega_M^{II} \le -1, \quad 2\tau_4\omega_M^{II} \ge -1, \tag{2.6}$$

$$\tau_1\omega_N^I - \tau_3\omega_M^{II} = 1, \quad \tau_2\omega_N^I - \tau_4\omega_M^{II} = 1. \tag{2.7}$$

Here we note that the scheme is stable even though the grid system is inhomogeneous, i.e., $N \neq M$.

Theorem 2.3 ([11]). *If each subdomain has the same domain interval Δ, then the stability conditions are given by, defining $\Delta_2 = 2/\Delta$,*

$$2\tau_1\omega_N^I \leq \Delta_2, \quad 2\tau_2\omega_N^I \geq \Delta_2, \quad 2\tau_3\omega_M^{II} \leq -\Delta_2, \quad 2\tau_4\omega_M^{II} \geq -\Delta_2,$$
$$\tau_1\omega_N^I - \tau_3\omega_M^{II} = \Delta_2, \quad \tau_2\omega_N^I - \tau_4\omega_M^{II} = \Delta_2.$$

Proof. The proof is done easily using the fact that for Ω^I,

$$(\vec{\omega}^I, \frac{\partial I_N^I f(q_N^I)}{\partial x})_N = \int_{-1}^{1} \frac{\partial I_N^I f(q_N^I)}{\partial x} d\xi$$
$$= \frac{2}{\Delta}\int_{-1}^{1} \frac{\partial I_N^I f(q_N^I)}{\partial \xi} d\xi = \frac{2}{\Delta}(f(0) - f(x_L)),$$

since $I_N^I f(q_N^I) \in P_{2N-1}$; and the same way for Ω^{II}. □

Theorem 2.4. *If the interval of each subdomain is different, then the scheme* (2.2) *is conservative if the following conditions are satisfied.*

$$\frac{\Delta^I}{2}\tau_1\omega_N^I - \frac{\Delta^{II}}{2}\tau_3\omega_M^{II} = 1, \quad \frac{\Delta^I}{2}\tau_2\omega_N^I - \frac{\Delta^{II}}{2}\tau_4\omega_M^{II} = 1. \tag{2.8}$$

Proof. Multiply the equations for q_N^I and q_M^{II} in (2.2) by $\vec{\omega}_N^I$ and $\vec{\omega}_M^{II}$. Then using the Legendre quadrature rule we have

$$\begin{aligned}
&\int_{x_L}^{0} \frac{\partial q_N^I}{\partial t} dx + \int_{0}^{x_R} \frac{\partial q_M^{II}}{\partial t} dx \\
&= -\int_{x_L}^{0} \frac{\partial f_N^I}{\partial x} dx - \int_{0}^{x_R} \frac{\partial f_M^{II}}{\partial x} dx + \frac{\Delta^I}{2}\tau_1\left[f^+(q_N^I(0,t))\omega_N^I - f^+(q_M^{II}(0,t))\omega_N^I\right] \\
&\quad + \frac{\Delta^I}{2}\tau_2\left[f^-(q_N^I(0,t))\omega_N^I - f^-(q_M^{II}(0,t))\omega_N^I\right] + \frac{\Delta^{II}}{2}\tau_3\left[f^+(q_M^{II}(0,t))\omega_0^{II} - f^+(q_N^I(0,t))\omega_0^{II}\right] \\
&\quad + \frac{\Delta^{II}}{2}\tau_4\left[f^-(q_M^{II}(0,t))\omega_0^{II} - f^-(q_N^I(0,t))\omega_0^{II}\right].
\end{aligned}$$

Using the fact that $\int \frac{\partial f_N}{\partial x} dx = f^+ + f^-$ and $\omega_0^{II} = \omega_M^{II}$, the RHS of the above equation without the boundary terms become

$$\begin{aligned}
RHS = {} & f^+(q_N^I(0,t))\left[\frac{\Delta^I}{2}\tau_1\omega_N^I - \frac{\Delta^{II}}{2}\tau_3\omega_M^{II} - 1\right] + f^+(q_M^{II}(0,t))\left[\frac{\Delta^{II}}{2}\tau_3\omega_M^{II} - \frac{\Delta^I}{2}\tau_1\omega_N^I + 1\right] \\
& + f^-(q_N^I(0,t))\left[\frac{\Delta^I}{2}\tau_2\omega_N^I - \frac{\Delta^{II}}{2}\tau_4\omega_M^{II} - 1\right] + f^-(q_M^{II}(0,t))\left[\frac{\Delta^{II}}{2}\tau_4\omega_M^{II} - \frac{\Delta^I}{2}\tau_2\omega_N^I + 1\right].
\end{aligned}$$

For any $f^{\pm}(0,t)$ (note that $f^{\pm}(q_N^I(0,t)) \neq f^{\pm}(q_M^{II}(0,t))$ in general), the RHS vanishes if the conditions in Eq. (2.8) are satisfied. □

Theorem 2.5. *The scheme* (2.2) *is stable if*

$$2\tau_1\omega_N^I \le \frac{2}{\Delta^I}, \quad 2\tau_2\omega_N^I \ge \frac{2}{\Delta^I}, \quad 2\tau_3\omega_M^{II} \le -\frac{2}{\Delta^{II}}, \quad 2\tau_4\omega_M^{II} \ge -\frac{2}{\Delta^{II}}, \tag{2.9}$$

$$\left(\tau_1\omega_N^I - \tau_3\omega_M^{II}\right)^2 - 2\left(\tau_1\omega_N^I\frac{2}{\Delta^{II}} - \tau_3\omega_M^{II}\frac{2}{\Delta^I}\right) + \frac{2}{\Delta^I}\frac{2}{\Delta^{II}} \le 0,$$

$$\left(\tau_2\omega_N^I - \tau_4\omega_M^{II}\right)^2 - 2\left(\tau_2\omega_N^I\frac{2}{\Delta^{II}} - \tau_4\omega_M^{II}\frac{2}{\Delta^I}\right) + \frac{2}{\Delta^I}\frac{2}{\Delta^{II}} \le 0, \tag{2.10}$$

Proof. Multiplying Eq. (2.2a) by $\vec{q}_N^I = (q_N^I(x_L),\cdots,q_N^I(0))^T$ and Eq. (2.2b) by $\vec{q}_M^{II} = (q_M^{II}(0),\cdots,q_M^{II}(x_R))^T$, then the energy

$$E(t) = \frac{2}{\Delta^I}\int_{x_L}^{0} q^2(x,t)dx + \frac{2}{\Delta^{II}}\int_0^{x_R} q^2(x,t)dx$$

satisfies

$$\begin{aligned}\frac{1}{2}\frac{dE(t)}{dt} = &\left(\tau_1\omega_N^I - \frac{2}{\Delta^I}\frac{1}{2}\right)\alpha_0^+ - (\tau_1\omega_N^I + \tau_3\omega_M^{II})\gamma_0^+ + \left(\tau_3\omega_M^{II} + \frac{2}{\Delta^{II}}\frac{1}{2}\right)\beta_0^+ \\ &+ \left(\tau_2\omega_N^I - \frac{2}{\Delta^I}\frac{1}{2}\right)\alpha_0^- - (\tau_2\omega_N^I + \tau_4\omega_M^{II})\gamma_0^- + \left(\tau_4\omega_M^{II} + \frac{2}{\Delta^{II}}\frac{1}{2}\right)\beta_0^-,\end{aligned}$$

where

$$\alpha_0^\pm = ((q_N^I(0,t))^T A^\pm q_N^I(0,t), \ \beta_0^\pm = (q_M^{II}(0,t))^T A^\pm q_M^{II}(0,t), \ \gamma_0^\pm = (q_N^I(0,t))^T A^\pm q_M^{II}(0,t).$$

To make the RHS less than or equal to zero, first, the coefficients of the 2nd-order terms corresponding to the positive flux (negative flux) should be non-positive (non-negative) which provides the conditions of Eq. (2.9). Also, the determinant for each of the quadratic equations should be non-positive. This provides the conditions of Eq. (2.10). □

Fig. 2 shows the stability regions for $\tau_1\omega_N^I$ and $\tau_2\omega_M^{II}$ with various Δ^{II} for which $\Delta^I = 2$ is used. When $\Delta^{II} = 2$, the stability region is simply a linear line shown as the blue straight line in the figure. As the domain size ratio between Ω^I and Ω^{II} increases the stability region becomes broader. The green and red dotted lines in the figure represent the boundaries of the stability region for $\Delta^{II} = 4$ and $\Delta^{II} = 10$, respectively. The black solid line represents the limit of the stability region, i.e., for $\Delta^{II} \to \infty$. The limit line is given by $(\tau_1\omega_N^I - \tau_3\omega_M^{II})^2 + 2\tau_3\omega_M^{II} \le 0$ and is independent of the value of Δ^{II}.

Remark 2.1. If $\tau_1 = \tau_4 = 0$, then the penalty interface conditions are basically the same as the upwind methods. If $\tau_1 = \tau_2$ and $\tau_3 = \tau_4$, then the scheme does not split the flux into the positive and negative ones but uses the flux itself in the penalty terms.

It is important to consider the averaging method with the inhomogeneous grid system since it is the popular and simplest interface conditions. For the averaging method,

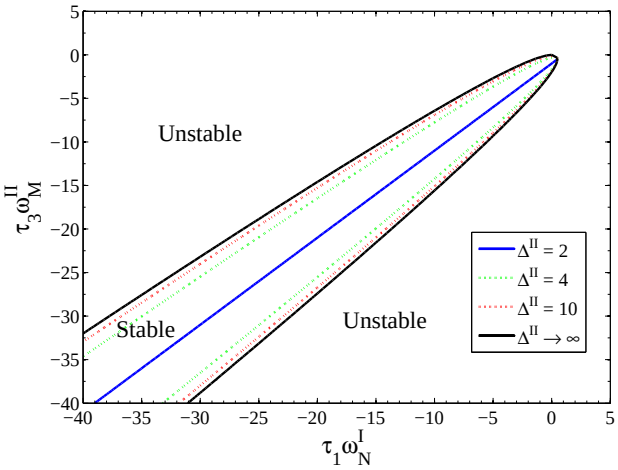

Figure 2: Stability regions for $\tau_1\omega_N^I$ and $\tau_2\omega_M^{II}$ with various Δ^{II} and $\Delta^I=2$.

the continuity of q at the interface is ensured. The averaging method is a special case of the penalty method. The averaging method has been effectively used in the previous work [11] for the homogeneous grid system. Since we assume that the boundary operators $\mathcal{B}$ and the spectral vanishing-viscosity SV ensure the stability at the boundaries $x=x_L$, and x_R, we consider only the contributions from the interface at $x=0$.

Now we consider the following penalty scheme for the averaging method

$$\begin{aligned}\frac{\partial q_N^I}{\partial t}+\frac{\partial I_N^I f(q_N^I)}{\partial x}&=\tau_1 Q_N(x)[f_x^+(q_N^I(0,t))-f_x^+(q_M^{II}(0,t))]\\&\quad+\tau_2 Q_N(x)[f_x^-(q_N^I(0,t))-f_x^-(q_M^{II}(0,t))],\\\frac{\partial q_M^{II}}{\partial t}+\frac{\partial I_M^{II} f(q_M^{II})}{\partial x}&=\tau_3 Q_M(x)[f_x^+(q_M^{II}(0,t))-f_x^+(q_N^I(0,t))]\\&\quad+\tau_4 Q_M(x)[f_x^-(q_M^{II}(0,t))-f_x^-(q_N^I(0,t))],\end{aligned}\tag{2.11}$$

where $f_x^{\pm}$ denotes the derivative $f^{\pm}$ with respective to x. The averaging method considered here is for the case that each subdomain can have different polynomial orders such as N and M for Ω^I and Ω^{II}, respectively. In [11], $N=M$ has been used for the averaging.

Theorem 2.6 (Averaging, [11]). *The scheme* (2.11) *is the averaging method if*

$$\tau_1=\tau_2=\tau_3=\tau_4=\frac{1}{2}.\tag{2.12}$$

Proof. If (2.12) is satisfied, then (2.11) becomes, at $x=0$,

$$\frac{\partial q_N^I}{\partial t}=\frac{\partial q_M^{II}}{\partial t}=-\frac{\partial}{\partial x}\left(\frac{1}{2}\left(I_N^I f(q_N^I)+I_M^{II} f(q_M^{II})\right)\right).\tag{2.13}$$

This completes the proof of the theorem. □

Theorem 2.7. *If* (2.12) *is satisfied, then the scheme* (2.11) *is conservative for any N and M, and* Δ^I *and* Δ^{II}.

Proof. By multiplying (2.11) by the weight vectors $\vec{\omega}_N^I$ and $\vec{\omega}_M^{II}$ and using the conditions (2.12) we have

$$\begin{aligned}\int_{x_L}^{0}\frac{\partial q_N^I}{\partial t}dx+\int_0^{x_R}\frac{\partial q_M^{II}}{\partial t}dx=&-\int_{x_L}^{0}\frac{\partial f_N^I}{\partial x}dx-\int_0^{x_R}\frac{\partial f_M^{II}}{\partial x}dx\\&+\frac{1}{2}\left[f_x(q_N^I(0,t))\frac{\Delta^I}{2}\omega_N^I-f_x(q_M^{II}(0,t))\frac{\Delta^{II}}{2}\omega_0^{II}\right]\\&+\frac{1}{2}\left[f_x(q_M^{II}(0,t))\frac{\Delta^{II}}{2}\omega_0^{II}-\frac{\Delta^I}{2}f_x(q_N^I(0,t))\omega_N^I\right].\end{aligned}$$

Thus ignoring the boundary contributions at $x=x_L$ and $x=x_R$, the RHS of the above equation becomes

$$RHS=-f_N^I(q_N^I(0,t))+f_N^{II}(q_M^{II}(0,t))=0. \tag{2.14}$$

Here we have used the fact that $q_N^I(0,t)=q_M^{II}(0,t)$ and $f_N^I(q_N^I(0,t))=f_N^{II}(q_M^{II}(0,t))$ from Theorem 2.6. □

Remark 2.2. The conditions of the penalty parameters obtained above are independent of the orders of each subdomain. Moreover, they are independent of the domain size as well.

Theorem 2.8. *With* (2.12) *the scheme* (2.11) *is not necessarily stable in general.*

Proof. By taking the discrete norms, the energy of (2.11), i.e.,

$$E(t)=\frac{2}{\Delta^I}\int_{x_L}^{0}q^2(x,t)dx+\frac{2}{\Delta^{II}}\int_0^{x^R}q^2(x,t)dx$$

becomes, without the boundary terms,

$$\begin{aligned}\frac{1}{2}\frac{dE(t)}{dt}=&-\frac{2}{\Delta^I}(q_N^I(0,t))^TAq_N^I(0,t)+\frac{2}{\Delta^{II}}(q_M^{II}(0,t))^TAq_M^{II}(0,t)\\&+(q_N^I(0,t)-q_M^{II}(0,t))\left[Aq_x^I-Aq_x^{II}\right]\\=&\left[\frac{2(\Delta^I-\Delta^{II})}{\Delta^I\Delta^{II}}\right](q_N^I(0,t))^TAq_N^I(0,t),\end{aligned}$$

where we have used that $q_N^I(0,t)=q_M^{II}(0,t)$ and $\tau_1=\tau_2=\tau_3=\tau_4=\frac{1}{2}$. Thus if $\Delta^I\neq\Delta^{II}$, the RHS does not necessarily non-positive. The RHS, however, vanishes if $\Delta^I=\Delta^{II}$ so that $E(t)=E(0)$. □

The continuity of q at the interface is ensured by using the averaging method (2.11). This, however, does not necessarily imply that the first derivative is also continuous at the interface. In general the first derivative is discontinuous, and the scheme is not stable.

2.2 Weighted spectral penalty method

In the previous section, it has been shown that the conservative and stable penalty method can be constructed for fully inhomogeneous grids, i.e., for $N \neq M$ and $\Delta^I \neq \Delta^{II}$ except the averaging method. The conditions obtained in the previous section are only *necessary* conditions. For example, the stability conditions, (2.6) and (2.7), suggest that the scheme (2.2) is stable if

$$\tau_1 = \tau_2 = \frac{1}{2\omega_N^I}, \quad \tau_3 = \tau_4 = -\frac{1}{2\omega_M^{II}}.$$

These conditions, albeit stable, can yield the nonphysical reflecting solutions at the inhomogeneous domain interfaces because the positive and negative fluxes are equally penalized as we will show in this section. In this section, the weighted spectral penalty method for the inhomogeneous grid is introduced to reduce such nonphysical modes at the domain interfaces.

With the weighted spectral penalty method, the incoming or outgoing characteristics are penalized with different weights if the inhomogeneous domain system is considered. That is, the incoming fluxes are penalized with the larger values of the penalty parameters than the outgoing fluxes. In the Legendre spectral penalty equation (2.2), the weighted spectral penalty method for Ω^I exploits

$$|\tau_2| \gg |\tau_1|, \tag{2.15}$$

and for Ω^{II}

$$|\tau_3| \gg |\tau_4|. \tag{2.16}$$

The numerical simulation results of the supersonic reactive cavity flow presented in this paper show that the upwind characteristic interface conditions are not enough to ensure the smooth solutions across the interfaces. We will show in the following sections that by weighting the incoming fluxes against the outgoing fluxes, the nonphysical modes in the solution at the domain interfaces can be reduced. The weight, however, can not be arbitrarily large due to the CFL restriction. In practice, we use the fixed weight for each penalty parameter. Since the problem considered in this paper is highly nonlinear, the fixed weight for any $t > 0$ may not be enough to prevent the growth at the interfaces. We use the local spectral vanishing viscosity method with the weighted penalty method to prevent any growth at the interfaces.

2.2.1 Reflection coefficients of the weighted penalty interface conditions

In order to explain how the weighted spectral penalty method can reduce the non-physical reflection modes, the reflection coefficients analysis is used. Consider the following simple linear hyperbolic equation

$$q_t + (Fq)_x = 0, \quad q : \mathbb{R} \times \mathbb{R} \to \mathbb{R}^2, \quad x \in \mathbb{R}, \quad t > 0, \tag{2.17}$$

where

$$q=\begin{pmatrix} u \\ v \end{pmatrix}, \qquad F=\begin{pmatrix} 0 & 1 \\ 1 & 0 \end{pmatrix}. \tag{2.18}$$

The same equation has been considered to show the reflecting modes at the domain interfaces with the spectral Galerkin method in [15]. We seek a wave solution such that

$$q(x,t)=\exp(i\omega t)\hat{q}(x), \qquad x\in[-2,2], \quad t\geq 0. \tag{2.19}$$

Plugging the wave solution into (2.18) yields

$$\hat{q}(x)=Aq_1\exp(-i\omega x)+Bq_2\exp(i\omega x), \tag{2.20}$$

where $q_1=(1,1)^T$ and $q_2=(1,-1)^T$.

Suppose that we have two subdomains $\Omega^I=[x_L,0]$, and $\Omega^{II}=[0,x_R]$, with $x_L<0$ and $x_R>0$. Let $\mathcal{B}^{\pm}$ be the boundary operators at the end points, i.e., $x=x_L$ and $x=x_R$. Moreover, f^+ and f^- are $f^{\pm}=F^{\pm}q=S\Lambda^{\pm}S^{-1}q$;

$$f^+=\frac{1}{2}\begin{pmatrix} u+v \\ u+v \end{pmatrix}, \qquad f^-=\frac{1}{2}\begin{pmatrix} -u+v \\ u-v \end{pmatrix}. \tag{2.21}$$

Here we assume that the boundary operator $\mathcal{B}$ is taken properly such that this treatment does not destroy the global stability and there is no reflection from the boundaries. In other words, we assume that we have the perfect and stable absorbing boundary operator at $x=x_L,x_R$. Plugging the wave solutions into the Legendre spectral method (2.2), we have the following linear system at the interface, i.e., at $x=0$,

$$\begin{aligned} &\tau_1(A^I-A^{II})-\tau_2(B^I-B^{II})=0, \quad \tau_3(A^{II}-A^I)-\tau_4(B^{II}-B^I)=0,\\ &\tau_1(A^I-A^{II})+\tau_2(B^I-B^{II})=0, \quad \tau_3(A^{II}-A^I)+\tau_4(B^{II}-B^I)=0. \end{aligned}$$

The above linear systems can be rewritten in the matrix form $\mathbf{WX}=\mathbf{ZX}$ with

$$\mathbf{X}=\begin{pmatrix} A^I \\ B^I \\ A^{II} \\ B^{II} \end{pmatrix}, \quad \mathbf{W}=\begin{pmatrix} -\tau_1 & \tau_1 & 0 & 0 \\ -\tau_2 & \tau_2 & 0 & 0 \\ 0 & 0 & -\tau_3 & \tau_3 \\ 0 & 0 & -\tau_4 & \tau_4 \end{pmatrix}, \quad \mathbf{Z}=\begin{pmatrix} 0 & 0 & -\tau_1 & \tau_1 \\ 0 & 0 & -\tau_2 & \tau_2 \\ -\tau_3 & \tau_3 & 0 & 0 \\ -\tau_4 & \tau_4 & 0 & 0 \end{pmatrix}.$$

The system is not well-posed as $\det(\mathbf{W}-\mathbf{Z})=0$. In fact this linear system can be solved by taking into account that A^{II} and B^{II} are considered as the given interface values for the solution of Ω^I and A^I and B^I of Ω^{II} in the real computation:

$$\tau_1A^I-\tau_2B^I=0, \qquad \tau_1A^I+\tau_2B^I=0.$$

Since A is corresponding to the outgoing flux and B to the incoming flux at $x=0$, respectively, define the reflection coefficients R_0 at $x=0$ for Ω^I

$$R_0=\left|\frac{B^I}{A^I}\right|=\left|\frac{\tau_1}{\tau_2}\right|. \tag{2.22}$$

We shall consider four different cases as given in Table 1, cases T-1 through T-4. By definition, there is no reflection at the interface for the case T-1, the upwind method. For the case T-2, we do not split the flux

$$\tau_1 f^+ + \tau_2 f^- = \tau(f^+ + f^-) = \tau f. \tag{2.23}$$

Consequently, the reflection is obvious although the method is simple. The case T-3 is the weighted penalty method. The case T-4 weights the outgoing flux against the incoming flux.

Table 1: Interface conditions and reflection coefficients.

Case	Interface conditions	Reflection coefficients
T-1	$\tau_1 = 0$	$R_0 = 0$
T-2	$\tau_1 = \tau_2 = \tau$	$R_0 = 1$
T-3	$\tau_1 \ll \tau_2$	$R_0 \ll 1$
T-4	$\tau_1 \gg \tau_2$	$R_0 \gg 1$

For illustration, consider a step function, i.e.,

$$u = v = \begin{cases} 1 & x \in \Omega^I, \\ 0 & x \in \Omega^{II}. \end{cases}$$

Fig. 3 shows the solutions after one time integration at $t = \Delta t = 0.0001$ for each case in Table 1. $\tau_1 = \tau_2 = \frac{1}{2\omega_N}$ are used for the case T-2, $\tau_2 \sim \mathcal{O}(N^3)$ and $\tau_1 \sim \mathcal{O}(N^2)$ are used for the case T-3 and $\tau_1 \sim \mathcal{O}(N^3)$ and $\tau_2 \sim \mathcal{O}(N^2)$ are used for the case T-4. Note the different behaviors between the case T-3 and the case T-4. For the case T-3 the penalty parameters associated with the incoming flux are weighted while the outgoing flux are weighted for the case T-4. The solution for the case T-3 does not show the overshoot at the interface for Ω^I. For the case T-4, the solution of Ω^I at the interface shows the overshoot. The behaviors of the interface solution of Ω^{II} for each case can be explained by taking into account that the scheme is in fact conservative.

2.2.2 Reflection and instability

We consider more numerical examples to confirm the performance of the weighted spectral penalty method.

Homogeneous grid. First consider the same wave equation with the following boundary conditions

$$\mathcal{B}q := \begin{cases} u(x,t) - v(x,t) = 0, & x = 4, \\ u(x,t) + v(x,t) = 0, & x = 0. \end{cases} \tag{2.24}$$

Here we consider two subdomains $\Omega^I = [0,2]$ and $\Omega^{II} = [2,4]$ with the same polynomial order N. For the boundary conditions at $x=0$ and $x=4$, we use the non-reflecting boundary conditions. The spectral penalty method (2.2) described in the above section is used with the Legendre polynomials.

(a) T-1: $\tau_1 = 0$ (b) T-2: $\tau_1 = \tau_2 = \frac{1}{2\omega_N}$

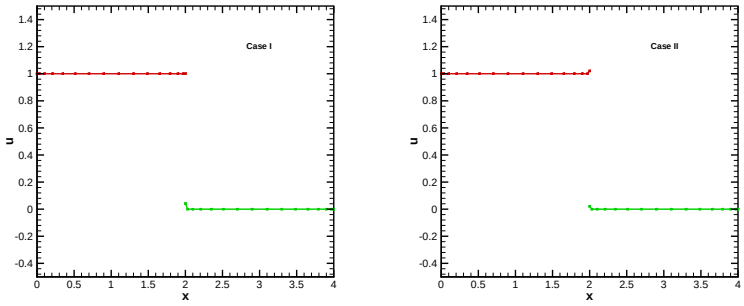

(c) T-3: $\tau_2 \sim \mathcal{O}(N^3)$ (d) T-4: $\tau_1 \sim \mathcal{O}(N^3)$

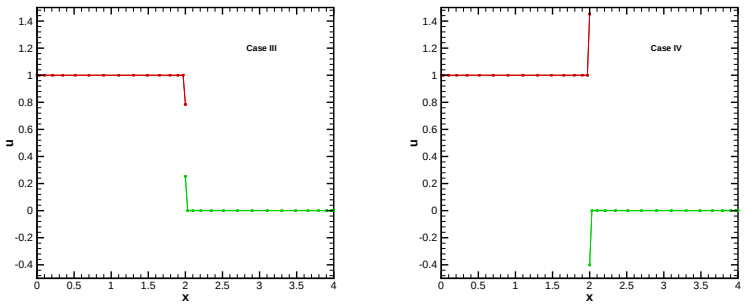

Figure 3: Shock calculation at the first time step.

We denote M-A, M-UW, M-NFS and M-WP by the averaging, upwind, no-flux splitting and the weighted penalty methods, respectively. They are listed in the following table.

Method	Interface Conditions	Remark
M-A	$\tau_1 = \tau_2 = \tau_3 = \tau_4 = \frac{1}{2}$	Averaging Method
M-UW	$\tau_1 = \tau_4 = 0, \tau_2 = -\tau_3 = \frac{1}{\omega_N}$	Upwind Method
M-NFS	$\tau_1 = \tau_2 = -\tau_3 = -\tau_4 = \frac{1}{2\omega_N}$	No-flux-Splitting Method
M-WP	$\mathcal{O}(\tau_2) = \mathcal{O}(\tau_3) \sim N^3, \tau_1 \neq 0 \neq \tau_4$	Weighted Penalty Method

Remark 2.3. Note that all four methods satisfy the stability conditions as each subdomain has the same polynomial order N and domain length $\Delta = 2$.

The CFL condition is given by

$$\min_i \frac{\Delta t}{\Delta x_i} \leq C_{FL}, \tag{2.25}$$

where C_{FL} is a positive constant and taken to make Δt be small enough for every case.

Table 2: The maximum error (L_∞) for M-A, M-UW, M-NFS and M-WP at time $t=1.5$.

N\Method	M-A	M-UW	M-NFS	M-WP
4	0.67	0.82	0.13E+01	0.74
8	0.65E-02	0.28E-02	0.82E-02	0.57E-02
16	0.34E-09	0.38E-09	0.65E-09	0.29E-09
32	0.52E-11	0.52E-11	0.52E-11	0.52E-11
64	0.54E-11	0.51E-11	0.54E-11	0.50E-11

Table 2 shows the L_∞ error for each method. The overall performance is almost the same for each method while the M-WP performs slightly better than the other methods.

Inhomogeneous grid. Now we consider the same problem with 3 subdomains, each of them having the same domain intervals, i.e., $\Omega^1=[0,2],\Omega^2=[2,4]$ and $\Omega^3=[4,6]$. For these three subdomains, consider the following two different cases:

Case	Grid resolution
C-1 (homogeneous)	$N_1=N_2=N_3=8$
C-2 (inhomogeneous)	$N_1=8,N_2=32,N_3=8$

Remark 2.4. Note that every method satisfies the stability condition for the case C-1. For the case C-2, only the M-A, which is the averaging method, does not satisfy the stability condition as explained in Section 2.1, but the M-NFS still satisfies the stability condition.

Table 3 shows the global L_∞ error for each case. As shown in the table, the M-A and the M-NFS show the instability at the interfaces for the case C-2. Table 4 shows the L_∞ error for Ω^2 for each case. The L_∞ error for Ω^2 is less than that of global L_∞ error for the M-UW and the M-WP of the case C-2 because the higher polynomial order of N is used.

Table 3: The maximum error (L_∞) for the case C-1 and the case C-2 at time $t=1.5$.

Case\Method	M-A	M-UW	M-NFS	M-WP
C-1	0.83E-02	0.29E-02	0.11E-01	0.52E-02
C-2	unstable	0.25E-02	unstable	0.65E-02

Table 4: The maximum error (L_∞) of Ω^2 for C-1 and C-2 at time $t=1.5$.

Case\Method	M-A	M-UW	M-NFS	M-WP
C-1	0.83E-02	0.29E-02	0.10E-01	0.51E-02
C-2	unstable	0.13E-02	unstable	0.51E-02

The instabilities of the M-A and the M-NFS are illustrated in Fig. 4. In the figure, the top figures represent the solution with M-A at $t=0.4$ and the bottom figures the solution with M-NFS at $t=1.5$. The left figures show $u+v$ and the right $u-v$. As shown in the figures, the locations of the instability are different for the M-A and the M-NFS. Since

$N_2 > N_1 = N_3$, there exist higher modes in Ω^2 which do not appear in the approximations for both Ω^1 and Ω^3. For the M-A, i.e., the averaging method, the figure indicates that the instability occurs at the interface of Ω^1 and Ω^2 for $u+v$, and the instability at the interface of Ω^2 and Ω^3 for $u-v$. This implies that the growth at the interface occurs when the characteristic of the lower modes enters the subdomain where the higher modes appear in the approximation. For the M-NFS, the growth occurs at different locations. If the outgoing characteristic is approximated with the higher modes, such modes in the approximation are reflected as if the adjacent subdomain plays a role as a wall boundary. The subdomain Ω^2 yields a free boundary condition for the lower mode wave solutions entering Ω^2. No significant growth at the interface is observed for the weighted penalty method.

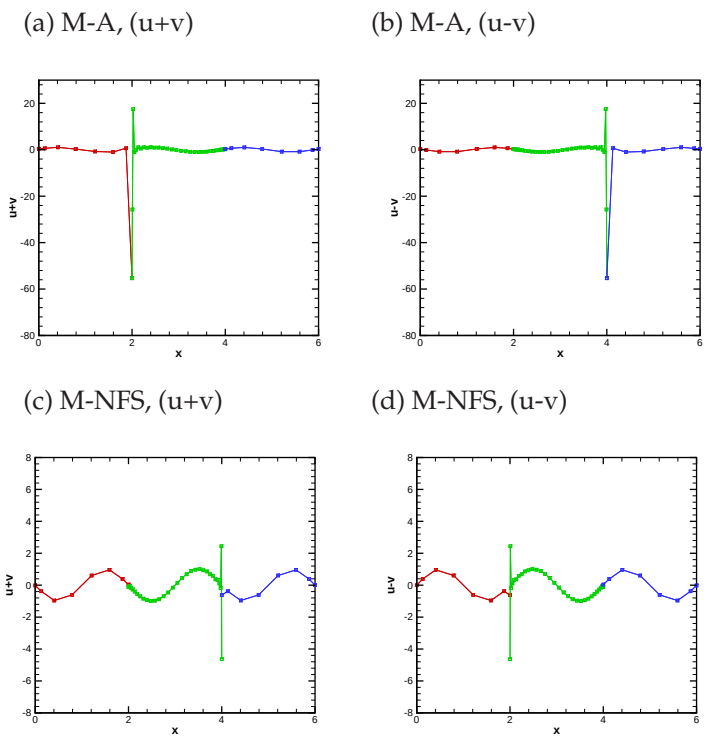

Figure 4: Solutions for the M-A at time $t=0.4$ and the M-NFS at time $t=1.5$. The $u+v$ and $u-v$ characteristic waves are shown in the left and right columns, respectively.

2.2.3 Adaptive super-viscosity method

As mentioned above, we use the fixed weight for each penalty parameter for the real computation. This is not enough for preventing the growth at the interface if the grid system is highly inhomogeneous. The super-viscosity method is used at the interface when the weighted penalty method fails to reduce the nonphysical growing modes. The super-viscosity method is only applied when and where it is necessary. Since the

nonphysical reflecting or growing modes are mainly contained in the higher modes, the super-viscosity can be used to remove such higher modes locally at the interface. This technique is critical for the stabilization of the multi-domain spectral penalty method for nonlinear problems.

For the numerical experiment, we revisit the simple wave problem used in [5],

$$\begin{cases} \frac{\partial u}{\partial t}+\frac{\partial u}{\partial x}=0 & x\in\Omega=(a,b), \quad t>0, \\ u(a,t)=u_L(t) & t>0, \\ u(x,0)=\cos(\pi x) & x\in\Omega. \end{cases} \tag{2.26}$$

We seek an approximation of u with two subdomains, $\Omega^1=[0,2]$ and $\Omega^2=[2,4]$ with $N_1\neq N_2$.

Two different cases are examined for the M-A and the M-NFS:

Case	Grid resolution
C-3	$N_1=32, N_2=8$
C-4	$N_1=8, N_2=32$

Table 5 shows the L_∞ errors of the case C-3 and the C-4. The table shows that these methods are stable in either case except the M-A and the M-NFS. Both of them are unstable if $N_1<N_2$ and $N_2<N_1$, respectively.

Table 5: The maximum error (L_∞) for C-3 and C-4 at time $t=1.5$.

Case/Method	M-A	M-UW	M-NFS	M-WP
C-3	0.13E-01	0.46E-02	4.89 (Unstable)	0.49E-02
C-4	0.54E+17 (Unstable)	0.46E-02	0.461E-02	0.46E-02

To avoid the growth in time, one can either use the explicit filtering method or add the super-vanishing viscosity (SV) term to the equation, namely,

$$\frac{\partial u_N}{\partial t}+\frac{\partial u_N}{\partial x}=\frac{1}{N^{2s-1}}\left[\frac{\partial}{\partial x}(1-x^2)\frac{\partial}{\partial x}\right]^s u_N+PT \qquad x\in\partial\Omega, \tag{2.27}$$

where N is the order of approximation, s is a positive integer growing with N [16,22] and PT denotes the penalty term. This SV method is equivalent to the filtering method [16,22] and we use the filtering method in this work instead of the SV. The exponential filter method with the filtering order γ is used for the numerical experiment. The exponential filter function $\sigma(k)$ and the filtering order γ are defined as $\sigma(k)=\exp(-\epsilon_M(k/N)^\gamma)$ where k is the mode number $k=0,\cdots,N$ and N is the polynomial order. The positive constant ϵ_M is chosen such that $\sigma(N)$ becomes machine zero. Typically $\epsilon_M\sim 32$.

Table 6 shows the results for the M-A and the M-NFS with the different orders of filtering γ. As the table indicates, no significant growth has been observed. Comparing with the results in Table 2, however, we notice that the filtering method permits a loss

Table 6: The maximum error (L_∞) for the reconstruction method.

	(M-A/C-4) (Ω^1)	(M-NFS/C-3) (Ω^2)
$\gamma=2$	1.13	0.18
$\gamma=4$	0.66	0.11E-01
$\gamma=8$	0.21	0.11E-01
$\gamma=16$	0.76E-01	0.11E-01
$\gamma=16^3$	0.15E-01	0.11E-01

Table 7: The maximum error (L_∞) for the reconstruction method ; $\gamma=16$.

	(M-A/C-4) (Ω^1)	(M-NFS/C-3) (Ω^1)
$N=4$	1.24	1.00
$N=8$	0.76E-01	0.11E-01
$N=16$	0.47E-06	0.12E-08
$N=32$	0.74E-11	0.52E-11

of accuracy. For example, the L_∞ error of M-NFS/C-3($N=(32,8)$) is 0.11×10^{-1} and M-NFS/C-4 ($N=(8,32)$) is 0.46×10^{-2}. Table 6 also indicates that the methods are stable even though $\gamma\to\infty$, which implies that stability can be achieved even with the small viscosity added.

Fixing the filtering order $\gamma=16$, Table 7 shows the full recovery of the accuracy as N increases, as the grid system becomes homogeneous.

We note that for the 2D problem, one needs to find the proper conditions for the corner of each subdomain. Such conditions will be investigated in our future work. The 2D numerical experiments based on the 1D method indicate, however, that the proposed method with the SV method applied at the interfaces and corners yields a stable and accurate result as shown in the next sections.

3 Injector-cavity scramjet system

In this section, the proposed weighted spectral penalty method is applied for the approximation of the supersonic flow interactions in the cavity-injector system with the inhomogeneous grid system. To refine the localized injector field, we use the narrow subdomain for the injector. The polynomial order of each domain is the same for both x- and y-directions. Thus the grid inhomogeneity in this case comes from the different domain length.

3.1 The cavity system and the governing equations

Cavities have been actively used as flame-holders in scramjet engines (see the review by Ben-Yakar and Hanson [4]). The injector-cavity system is illustrated in Fig. 1 (left figure). The cavity system is categorized into 4 different types such as open, closed,

transitional-closed and transitional-open depending on the length scale of cavity [4]. The cavity system with the length-to-depth ratio $L/D < 7 \sim 10$ is called an open cavity as the upper shear layer reattaches itself at the back face. Under the shear layer formed over cavity, the flows with the hydrogen fuel are possibly captured inside cavity and generate the recirculation zone. The generated recirculation interacts with the shear layer and the acoustic waves inside cavity. The radicals from the chemical reaction between the hydrogen and oxygen gases reside inside cavity and trigger the auto-ignition of the supersonic engine. In principle, the more stable and longer recirculation is maintained, the more efficient fuel performance can be achieved.

The major question of the cavity flame-holder system that needs to be investigated is: *How does the fuel injection interact with cavity flows?* There have been many numerical studies on the recirculation and stabilizations of the flow inside cavity but rarely on how the continuous supply of the fuel can affect the flow dynamics inside cavity [2,3,7,23,24, 27,28]. Since the injection of the fuel in the combustor is necessary, the injection emerges as another important key parameter for the optimal configuration of the cavity flame-holder. Both comprehensive laboratory and numerical experiments have to be carried out to answer the question. In this work, we use the length-to-depth ratio $L/D = 4\text{cm}/1\text{cm} = 4$, that is, we use the open cavity.

The governing equations are the compressible 2D reactive Navier-Stokes equations with the chemical source terms given by

$$\frac{\partial q}{\partial t} + \frac{\partial F}{\partial x} + \frac{\partial G}{\partial y} = \frac{\partial F_v}{\partial x} + \frac{\partial G_v}{\partial y} + C, \tag{3.1}$$

where $q = (\rho, \rho u, \rho v, E, \rho \mathbf{f})^T$ is the state vector, $F = (\rho u, \rho u^2 + P, \rho uv, (E+P)u, \rho \mathbf{f} u)^T$ and $G = (\rho v, \rho uv, \rho v^2 + P, (E+P)v, \rho \mathbf{f} v)^T$ the inviscid fluxes, F_v and G_v the viscous fluxes and C the chemical source term, respectively. Here ρ, u, v, E, P, and $\mathbf{f}$ denote the density, the velocity in x-direction and the velocity in y-direction, the total energy, the pressure and the mass fraction vector, respectively. The chemical model uses four chemical species, H_2, O_2, H_2O and N_2 with the reversible chemical reaction between hydrogen and oxygen gases given by

$$2H_2 + O_2 \rightleftharpoons 2H_2O. \tag{3.2}$$

A modified Arrhenius law gives the equilibrium reaction rate k_e, the forward reaction rate k_f and the backward reaction rate k_b as

$$\begin{aligned} k_e &= A_e T \exp(4.60517(E_e/T - 2.915)), \\ k_f &= A_f \exp(-E_f/(RT)), \\ k_b &= k_f/k_e, \end{aligned}$$

where $E_e = 12925$, and $E_f = 7200$ are the activation energy and $A_e = 83.006156$, and $A_f = 5.541 \times 10^{14}$ are the frequency factors. R is the universal gas constant. Each chemical species has different dynamical viscosity μ_i based on the Sutherland's law. The mixture

viscosity μ is obtained according to the Wilke's law [26]. The Prandtl number Pr and the Schmidt number Sc are taken to be 0.72 and 0.22 respectively for the normal air. The equation of state is given by the assumption of the perfect gas law. Detailed formulation of the equations can be found in [9,11].

With L fixed we consider two different angles of the aft wall, i.e., 90° and 30°. For the fluid conditions, the free stream Mach number $M=1.91$, total pressure $P=2.82$atm, total temperature $T=830.6$K and normalized Reynolds number $R_e=3.9\times10^7\text{m}^{-1}$ are used. Note that the Reynolds number is normalized and has the unit of $1/[length]$, and that the Reynolds number based on the cavity dimensions is about $\mathcal{O}(10^5)$. The boundary layer thickness scale is $\delta=5\times10^{-4}$m, and the wall temperature is $T_w=460.7835$K. For more detailed physical configuration and its explanation, we refer [11]. The hydrogen fuel is injected 1.5cm ahead of the cavity with the injection Mach number $M=1$ (see Figure 1). The numerical experiments are conducted with two different sizes of the injector diameter, $d=2$mm and $d=2$cm to investigate the effect of the injector-channel flow interactions on the development of the shear layer over cavity. The fuel is injected into the channel flow with the direction normal to the base wall. The total pressure and the total temperature of the hydrogen jet are 2.828522atm and 830.6K respectively.

3.2 Grid inhomogeneity and the weighted penalty method

To deal with the grid inhomogeneity we use the weighted penalty method described in Section 3. The weighted penalty method is based on the characteristic decomposition and it does not modify the stability conditions associated with $\mathbf{A}_v\cdot\mathbf{q}$ and $\mathbf{A}_v\cdot\partial\mathbf{q}$ for the Navier-Stokes equations in [11].

Fig. 5 shows the effect of the grid inhomogeneity on the solution. The subdomain containing the injector has a smaller domain length than other subdomains. The left figure shows the solution based on the averaging method (M-A) and the right shows the solution based on the weighted penalty method (M-WP). The figures clearly show that the averaging interface condition (M-A) yields a nonphysical concentration near the domain interface while the weighted penalty interface condition (M-WP) yields smooth solutions across the interfaces. We note that if the penalty parameters corresponding to the incoming and outgoing fluxes are of the same order satisfying the stability and conservativity conditions, the similar results are obtained as those with the averaging method. Thus the weighted penalty method is necessary.

Fig. 6 shows the flow fields near the injector subdomain with the weighted penalty method. The figure shows the flow streamline near the injector. The figure shows that there is no significant reflection at the injector subdomain interfaces. It is also shown that the flow fields are well resolved with the weighted penalty method. The small recirculation formed in front of the injector is clearly seen. Such recirculation is physically formed due to the interaction between the incoming channel flow and the hydrogen jet with the no-slip boundary condition at the wall [3,4].

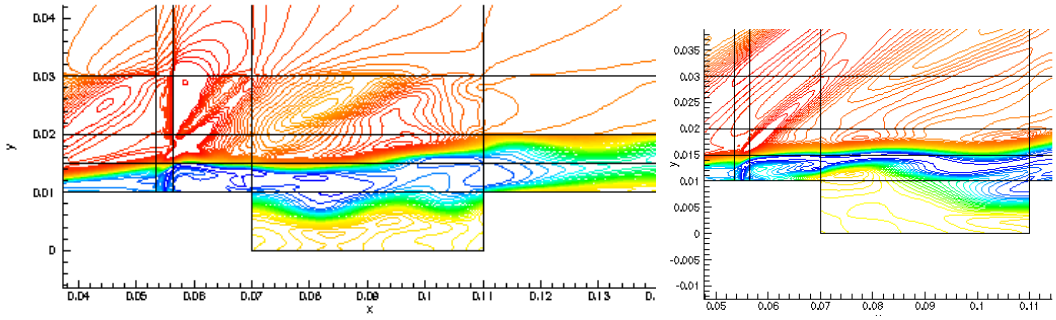

Figure 5: Density contour of injector-cavity-channel flow by reactive Navier-Stokes equations for the normal cavity flame-holder. Each subdomain has the same polynomial order for the approximation, that is, each subdomain has N grid points both in x- and y-directions but the different subdomain length. The left figure shows the solution using the averaging interface conditions (M-A) and the right figure shows the solution using the weighted penalty interface conditions (M-WP). The weighted penalty interface condition method considerably reduces the nonphysical density concentration near the interfaces seen in the left figure.

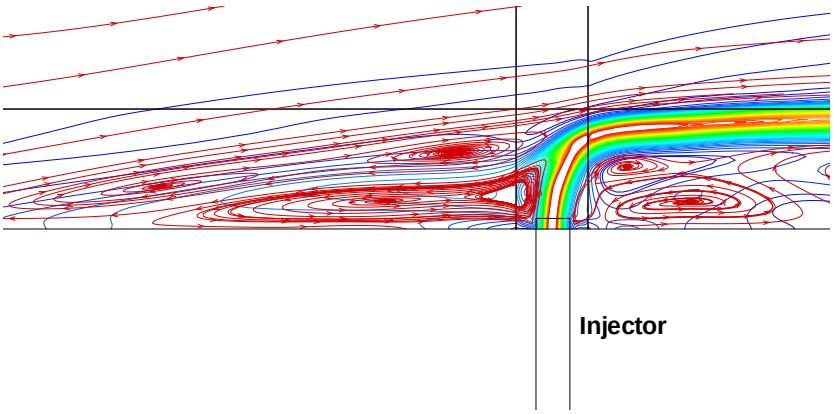

Figure 6: The recirculation zones formed in front of the hydrogen jet: the flow streamlines are given with the hydrogen jet contour for the narrow injector-cavity system at $t=0.225$ms.

3.3 Shear layer interactions

One of the major effects on the stability of the recirculation zone is by the shear layer over cavity. In [4] (also see references therein), several effects on the shear layer formation and its interaction with the cavity have been discussed including the location, size and the total number of injectors. Fig. 7 shows the water contours for both narrow and broad injectors. By placing the injector in front of the cavity front wall, the pressure fluctuations are reduced and the sharp gradients found near the corner of the aft wall are also weakened as the shear layer is being developed. The figures show that the broader injector has more enhanced shear layer growth over the cavity than the narrow jet. However, the pressure profiles in Fig. 9 indicate that the pressure oscillations are attenuated with

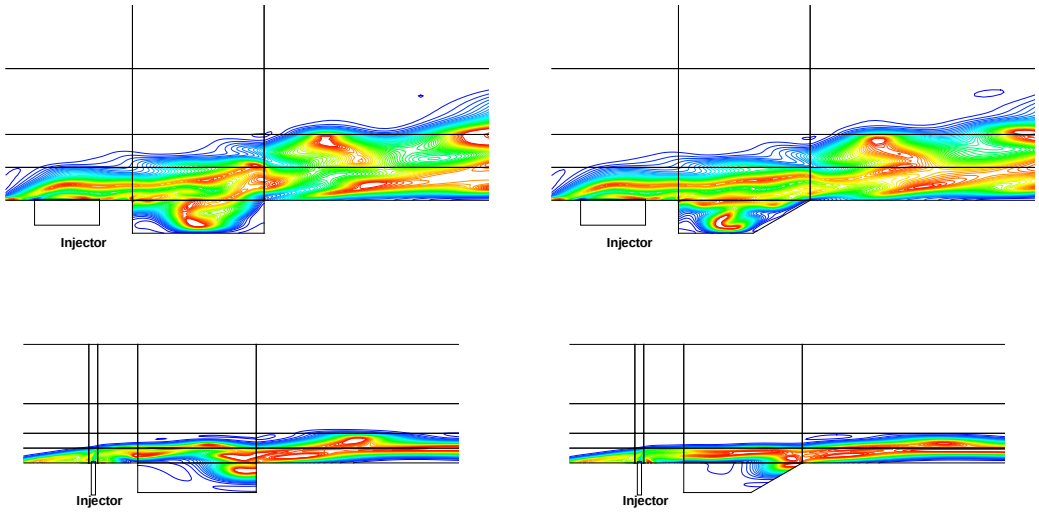

Figure 7: Water production and transport for 90° and 30° cavity walls: the upper figures shows the broad injector-cavity system and the bottom figures the water contours of the narrow injector-cavity system at $t=0.225$ms, respectively. There are 50 contour levels ranged from -0.001 to 0.23.

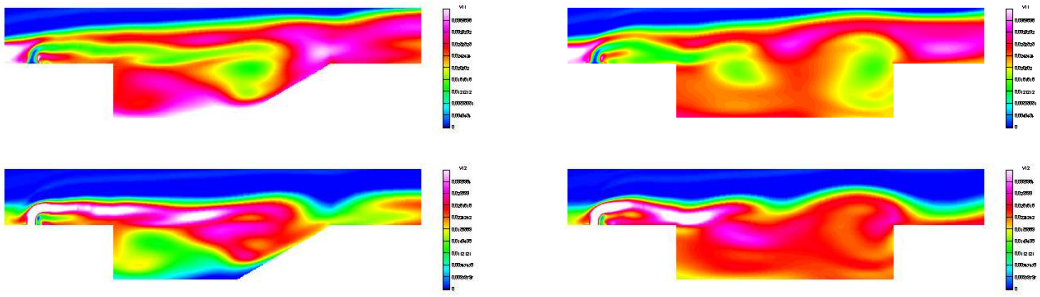

Figure 8: Water and hydrogen density profiles at $t=3.48$ms for the narrow injector-cavity system with 30° and 90° aft walls. The top figures show the water density contours and the bottom figures the hydrogen density contours.

the narrow injector more than the broad injector. This implies that there exists an optimal size of the injector with the fixed location of the injector from the front cavity wall that minimizes the pressure fluctuations and maximizes the stability of the recirculation zones inside cavity. Both the broad and narrow injector systems also show that they have weaker flow gradients near the aft wall than the flow gradients obtained in our previous work without the injector. The injection angle is normal to the wall but different injection angles can be used. In [3, 4], it has been discussed that the angled injector such as 30° or 60° can further weaken the possible bow shock found at the aft wall. Fig. 8 shows some detailed differences of the water and hydrogen profiles between the normal and recessed cavities at $t=3.48$ms for the narrow injector system.

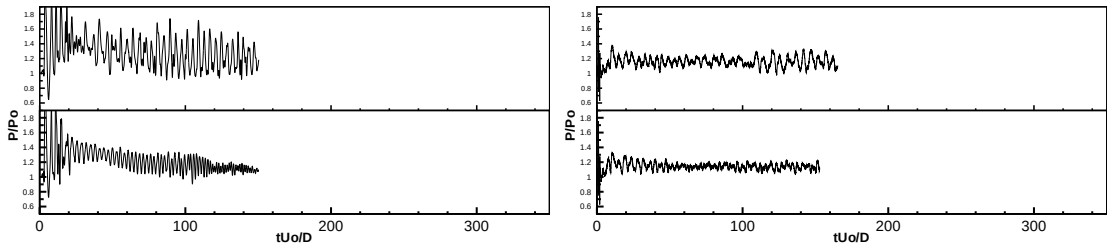

Figure 9: Pressure history for broad (left) and narrow (right) injector-cavity flows at the center of cavity. For the broad jet, the diameter is $d=2$cm and $d=2mm$ for the narrow jet. Each panel shows the case of 90° and 30° cavity walls from top to bottom.

3.4 Pressure fluctuations

In [11], we considered the cold and reactive flows without the hydrogen injector and showed that the pressure fluctuations inside cavity can be considerably reduced if the aft wall is slanted. Consequently this helps more stable recirculation inside cavity to be developed. The generated acoustic waves disturbing the recirculation are reflected back to the shear layer due to the slantness of the rear wall. Similar results are found in the cavity system with the injection fields. Fig. 9 shows the pressure fluctuation history profiles for the normal (90°, top figures) and slanted wall (30°, bottom figures) cases for the broad (left) and narrow (right) injectors. In the figures, the pressure fluctuations are measured up to $tU_o/D\sim150$ but plotted in the same scale used in Fig. 6 of [11] for the comparison. The pressures are measured at the center of cavity. For the broad injector-cavity system, it is clearly shown that the pressure fluctuations are much attenuated for the lower aft wall case and these features are similar to those for the non-reactive cold flow cases. For the narrow injector-cavity system, the pressure fluctuations for both 90° and 30° wall cavities are highly attenuated compared to those for the broad injector-cavity system. The differences of the pressure fluctuations between 30° and 90° are not significant, but one can observe that the lower angled wall cavity has less pressure fluctuations than the normal wall cavity. These results are similar to those for the reactive flow cases without the injection field. Note that the pressure fluctuations of the normal wall cavity system are also much attenuated compared to the pressure fluctuation of the normal wall cavity system without the injection field. This result shows that the injection field in front of the cavity increases the stability of the recirculation inside cavity.

4 Summary

In this research, the direct numerical simulation of the supersonic injector-cavity scramjet system has been carried out with the multi-domain spectral penalty method with the inhomogeneous grid system. In order to minimize the development of the nonphysical modes in the solution generated at the domain interfaces due to the grid inhomogeneity, we first derived the stable and conservative interface conditions of the multi-domain

spectral penalty method. For general inhomogeneous grid system, it is shown that it is possible to construct a stable and conservative spectral penalty method. It is also shown that the conservativity can be preserved but the stability is not maintained for the averaging method in general. The weighted penalty interface conditions is then proposed to minimize the non-physical effect at the inhomogeneous grid interfaces. The weighted penalty method gives more weight to the incoming fluxes than the outgoing fluxes. The reflection analysis shows that the weighted penalty method reduces the reflections at the domain interface by weighting the incoming fluxes. For the numerical experiments, we use the fixed weight for all time. The weight, however, can be adaptively determined depending on the flow conditions. Such adaptivity will be investigated in our future work. The weighted penalty method reduces the nonphysical growth at the domain interface considerably but not completely. The adaptive filtering method is used together with the weighted penalty method to stabilize any growth at the interface. The adaptive filtering is only applied at a small number of points at the interface. The direct numerical simulation shows that the proposed method successfully yields a stable and accurate approximation of the injector-cavity flows with the inhomogeneous grids. It is qualitatively shown that the recessed cavity yields a better performance of the pressure fluctuation reduction and enhances the stability of the recirculation zones inside cavity. The injector located in front of the cavity also reduces the pressure fluctuations inside cavity. More detailed geometric configurations maximizing the attenuation of the pressure fluctuations and the stability of the recirculation inside cavity will be investigated in our future work. The future research work will also center around the development of the 3D spectral penalty method with the weighted penalty conditions.

Acknowledgments

The first (WSD) and second authors (DG) gratefully acknowledge the support of this work by the AFOSR under contract number FA9550-08-1-0200 and DOE under contract number DE-FG02-98ER25346. The third author (JHJ) has been supported by the NSF under Grant No. DMS-0608844. The authors also thank the anonymous referees for their careful reading and helpful suggestions.

References

[1] R.A. Baurle and M.R. Gruber, A study of recessed cavity flowfields for supersonic combustion applications, AIAA-98-0938, 1998.
[2] R.A. Baurle, R.P. Fuller, J.A. White, T.H. Chen, M.R. Gruber and A.S. Nejad, An investigation of advanced fuel injection schemes for scramjet combustion, AIAA Paper 98-0937, 1998.
[3] R. A. Ben-Yakar and R. K. Hanson, Cavity flameholders for ignition and flame stabilization in scramjets: review and experimental study, AIAA-98-3122, 1998.
[4] A. Ben-Yakar and R. K. Hanson, Cavity flame-holders for ignition and flame stabilization in scramjets: an overview., J. Propul. Power **17** (4), 2001, 869-877.

[5] C. Canuto, M.Y. Hussaini, A. Quarternoni and T. Zang, Spectral Methods in Fluid Dynamics, Springer-Verlag, New York, 1987.
[6] M. H. Carpenter, D. Gottlieb, C.-W. Shu, ICASE 2001-44 (2001). On the conservation and convergence to weak solutions of global schemes, J. Sci. Comput. **18** (1), 2003, 111-132.
[7] D. L. Davis and R. D. W. Bowersox, Computational fluid dynamics analysis of cavity flameholders for scramjets, AIAA paper 97-3274 (1997).
[8] P. J. Diamessis, J. A. Domaradzki and J. S. Hesthaven, A spectral multidomain penalty method model for the simulation of high Reynolds number localized incompressible stratified turbulence, J. Comput. Phys. **202**, 2005, 298-322.
[9] W. S. Don and D. Gottlieb, Spectral simulation of supersonic reactive flows, SIAM, J. Numer. Anal. **35**, 1998, 2370–2384.
[10] W. S. Don and D. Gottlieb, High order methods for complicated flows interacting with shock waves, AIAA 97-0538 1997.
[11] W. S. Don, D. Gottlieb and J.-H. Jung, A multidomain spectral method for supersonic reactive flows, J. Comput. Phys. **192** (1), 2003, 325-354.
[12] W. S. Don and C. B. Quillen, Numerical simulation of shock-cylinder interactions I : resolution, J. Comput. Phys. **122**, 1995, 244–265.
[13] D. Funaro and D. Gottlieb, A new method of imposing boundary conditions in pseudospectral approximations of hyperbolic equations, Math. Comp. **51**, 1998, 599–613.
[14] D. Funaro and D. Gottlieb, Convergence results for pseudospectral approximations of hyperbolic systems by a penalty-type boundary treatment, Math. Comp. **57**, 1991, 585–596.
[15] S. Gottlieb and J.-H. Jung, Numerical issues in the implementation of high order polynomial multidomain penalty spectral Galerkin methods for hyperbolic conservation laws, Commun. Comput. Phys. **5**, 2009, 600-619.
[16] B. Y. Guo, H. Ma and E. Tadmor, Spectral vanishing viscosity method for nonlinear conservation laws, SIAM J. Numer. Anal. **39** (4), 2002, 1254–1268.
[17] J. S. Hesthaven and D. Gottlieb, A stable penalty method for the compressible Navier-Stokes equations. I. Open boundary conditions, SIAM J. Sci. Comp. **17**, 1996, 579–612.
[18] J. S. Hesthaven, A stable penalty method for the compressible Navier-Stokes equations II. One-dimensional domain decomposition schemes, SIAM J. Sci. Comput. **17**, 1997, 658–685.
[19] J. S. Hesthaven, A stable penalty method for the compressible Navier-Stokes equations. III. Multi dimensional domain decomposition schemes, SIAM J. Sci. Comp. **20** (1), 1999, 62–93.
[20] M. Latini, O. Schilling and W. S. Don, High-resolution simulations and modeling of reshocked single-mode Richtmyer-Meshkov instability. Part 1. Comparison to experimental data and to amplitude growth model predictions, Physics of Fluids, 19 (2), 2007, 1–19.
[21] M. Latini, O. Schilling and W. S. Don, High-resolution simulations and modeling of reshocked single-mode Richtmyer-Meshkov instability. Part 2. Physics of reshock and mixing, Physics Review E, **76**, 2007, 1–28.
[22] H. Ma, Chebyshev-Legendre super spectral viscosity method for nonlinear conservation laws, SIAM J. Numer. Anal. **35**, 1998, 893–908.
[23] D. P. Rizzetta, Numerical simulation of supersonic flow over a three-dimensional cavity, AIAA J. **26** (7), 1988, 799.
[24] M. B. Tracy and E. B. Plentovich, Characterization of cavity flow fields using pressure data obtained in the Langley 0.3-meter transonic cryogenic tunnel, NASA Technical Memorandum, 1993, 4436.
[25] H. Vandeven, Family of spectral filters for discontinuous problems, J. Sci. Comput. **6**, 1991, 159–192.

[26] C.R. Wilke, A viscosity equation for gas mixtures, J. Chem. Phys. **18**, 1950, 517–519.
[27] X. Zhang and J. A. Edwards, An investigation of supersonic cavity flows driven by thick shear layers, Aeronaut J. **94** (940), 1990, 355.
[28] X. Zhang, A. Rona and J. A. Edwards, The effect of trailing edge geometry on cavity flow oscillation driven by a supersonic shear layer, Aeronaut J. **102** (1013), 1998, 129.